

**Final results of Borexino on CNO solar neutrinos**

D. Basilico,<sup>9</sup> G. Bellini,<sup>9</sup> J. Benziger,<sup>13</sup> R. Biondi,<sup>8,\*\*</sup> B. Caccianiga,<sup>9</sup> F. Calaprice,<sup>12</sup> A. Caminata,<sup>3</sup>  
 A. Chepurinov,<sup>17</sup> D. D'Angelo,<sup>9</sup> A. Derbin,<sup>11</sup> A. Di Giacinto,<sup>8</sup> V. Di Marcello,<sup>8</sup> X. F. Ding,<sup>12,§</sup>  
 A. Di Ludovico,<sup>12,\*</sup> L. Di Noto,<sup>3</sup> I. Drachnev,<sup>11</sup> D. Franco,<sup>1</sup> C. Galbiati,<sup>12,18</sup> C. Ghiano,<sup>8</sup> M. Giammarchi,<sup>9</sup>  
 A. Goretti,<sup>12,\*</sup> M. Gromov,<sup>17,2</sup> D. Guffanti,<sup>20,‡</sup> Aldo Ianni,<sup>8</sup> Andrea Ianni,<sup>12</sup> A. Jany,<sup>4</sup> V. Kobychyev,<sup>5</sup>  
 G. Korga,<sup>23,24</sup> S. Kumaran,<sup>21,22,¶</sup> M. Laubenstein,<sup>8</sup> E. Litvinovich,<sup>6,7</sup> P. Lombardi,<sup>9</sup> I. Lomskeya,<sup>11</sup> L. Ludhova,<sup>21,22</sup>  
 I. Machulin,<sup>6,7</sup> J. Martyn,<sup>20</sup> E. Meroni,<sup>9</sup> L. Miramonti,<sup>9</sup> M. Misiaszek,<sup>4</sup> V. Muratova,<sup>11</sup> R. Nugmanov,<sup>6</sup> L. Oberauer,<sup>16</sup>  
 V. Orekhov,<sup>20</sup> F. Ortica,<sup>10</sup> M. Pallavicini,<sup>3</sup> L. Pelicci,<sup>21,22</sup> Ö. Penek,<sup>21,||</sup> L. Pietrofaccia,<sup>12,\*</sup> N. Pilipenko,<sup>11</sup>  
 A. Pocar,<sup>14</sup> G. Raikov,<sup>6</sup> M. T. Ranalli,<sup>8</sup> G. Ranucci,<sup>9</sup> A. Razeto,<sup>8</sup> A. Re,<sup>9</sup> N. Rossi,<sup>8</sup> S. Schönert,<sup>16</sup> D. Semenov,<sup>11</sup>  
 G. Settanta,<sup>21,†</sup> M. Skorokhvatov,<sup>6,7</sup> A. Singhal,<sup>21,22</sup> O. Smirnov,<sup>2</sup> A. Sotnikov,<sup>2</sup> R. Tartaglia,<sup>8</sup> G. Testera,<sup>3</sup>  
 E. Unzhakov,<sup>11</sup> F. L. Villante,<sup>8,25</sup> A. Vishneva,<sup>2</sup> R. B. Vogelaar,<sup>15</sup> F. von Feilitzsch,<sup>16</sup> M. Wojcik,<sup>4</sup> M. Wurm,<sup>20</sup>  
 S. Zavatarelli,<sup>3</sup> K. Zuber,<sup>19</sup> and G. Zuzel<sup>4</sup>

(Borexino Collaboration)

<sup>1</sup>*AstroParticule et Cosmologie, Université Paris Diderot, CNRS/IN2P3, CEA/IRFU, Observatoire de Paris, Sorbonne Paris Cité, 75205 Paris Cedex 13, France*

<sup>2</sup>*Joint Institute for Nuclear Research, 141980 Dubna, Russia*

<sup>3</sup>*Dipartimento di Fisica, Università degli Studi e INFN, 16146 Genova, Italy*

<sup>4</sup>*M. Smoluchowski Institute of Physics, Jagiellonian University, 30348 Krakow, Poland*

<sup>5</sup>*Institute for Nuclear Research of NASU, 03028 Kyiv, Ukraine*

<sup>6</sup>*National Research Centre Kurchatov Institute, 123182 Moscow, Russia*

<sup>7</sup>*National Research Nuclear University MEPhI (Moscow Engineering Physics Institute), 115409 Moscow, Russia*

<sup>8</sup>*INFN Laboratori Nazionali del Gran Sasso, 67010 Assergi (AQ), Italy*

<sup>9</sup>*Dipartimento di Fisica, Università degli Studi e INFN, 20133 Milano, Italy*

<sup>10</sup>*Dipartimento di Chimica, Biologia e Biotecnologie, Università degli Studi e INFN, 06123 Perugia, Italy*

<sup>11</sup>*St. Petersburg Nuclear Physics Institute NRC Kurchatov Institute, 188350 Gatchina, Russia*

<sup>12</sup>*Physics Department, Princeton University, Princeton, New Jersey 08544, USA*

<sup>13</sup>*Chemical Engineering Department, Princeton University, Princeton, New Jersey 08544, USA*

<sup>14</sup>*Amherst Center for Fundamental Interactions and Physics Department, University of Massachusetts, Amherst, Massachusetts 01003, USA*

<sup>15</sup>*Physics Department, Virginia Polytechnic Institute and State University, Blacksburg, Virginia 24061, USA*

<sup>16</sup>*Physik-Department, Technische Universität München, 85748 Garching, Germany*

<sup>17</sup>*Lomonosov Moscow State University Skobel'syn Institute of Nuclear Physics, 119234 Moscow, Russia*

<sup>18</sup>*Gran Sasso Science Institute, 67100 L'Aquila, Italy*

<sup>19</sup>*Department of Physics, Technische Universität Dresden, 01062 Dresden, Germany*

<sup>20</sup>*Institute of Physics and Excellence Cluster PRISMA+, Johannes Gutenberg-Universität Mainz, 55099 Mainz, Germany*

<sup>21</sup>*Institut für Kernphysik, Forschungszentrum Jülich, 52425 Jülich, Germany*

<sup>22</sup>*III. Physikalisches Institut B, RWTH Aachen University, 52062 Aachen, Germany*

<sup>23</sup>*Department of Physics, Royal Holloway University of London, Egham, Surrey, TW20 0EX, United Kingdom*

<sup>24</sup>*Institute of Nuclear Research (Atomki), Debrecen, Hungary*  
<sup>25</sup>*Dipartimento di Scienze Fisiche e Chimiche, Università dell'Aquila,*  
*67100 L'Aquila, Italy*



(Received 27 July 2023; accepted 25 September 2023; published 14 November 2023)

In this paper, we report the first measurement of CNO solar neutrinos by Borexino that uses the correlated integrated directionality (CID) method, exploiting the subdominant Cherenkov light in the liquid scintillator detector. The directional information of the solar origin of the neutrinos is preserved by the early Cherenkov photons from the neutrino scattered electrons and is used to discriminate between signal and background. The directional information is independent from the spectral information on which the previous CNO solar neutrino measurements by Borexino were based, except for the selection of the energy region of interest. While the CNO spectral analysis could only be applied on the Phase-III dataset, the directional analysis can use the complete Borexino data taking period from 2007 to 2021. The absence of CNO neutrinos has been rejected with  $> 5\sigma$  posterior probability using the Bayesian statistics. The directional CNO measurement is obtained without an external constraint on the  $^{210}\text{Bi}$  contamination of the liquid scintillator, which was applied in the spectral analysis approach. The final and the most precise CNO measurement of Borexino is then obtained by combining the new CID-based CNO result with an improved spectral fit of the Phase-III dataset. Including the statistical and the systematic errors, the extracted CNO interaction rate is  $R(\text{CNO}) = 6.7_{-0.8}^{+1.2}$  cpd/100 tonnes. Taking into account the neutrino flavor conversion, the resulting CNO neutrino flux at Earth is  $\Phi_{\text{CNO}} = 6.7_{-0.8}^{+1.2} \times 10^8 \text{ cm}^{-2} \text{ s}^{-1}$ , which is found to be in agreement with the high metallicity standard solar models. This outcome, combined with the  $^7\text{Be}$  and  $^8\text{B}$  fluxes measurements previously obtained by Borexino, can be used to disfavor the low metallicity SSM B16-AGSS09met model at  $3.2\sigma$  CL, assuming the SSM B16-GS98 high metallicity model to be true. Also, the sum of C and N abundances in the solar core with respect to the H abundance is evaluated with improved precision, resulting in  $N_{\text{CN}} = 5.81_{-0.94}^{+1.22} \times 10^{-4}$ , which is compatible with the high metallicity scenario and exhibits a  $2\sigma$  tension with the low metallicity case. The results described in this work reinforce the role of directional Cherenkov light in large-scale liquid scintillator detectors and open up new avenues for the next-generation liquid scintillator or hybrid neutrino experiments. A particular relevance is expected for the latter detectors, which aim to combine the advantages from both Cherenkov-based and scintillation-based detection techniques.

DOI: [10.1103/PhysRevD.108.102005](https://doi.org/10.1103/PhysRevD.108.102005)

## I. INTRODUCTION

Solar neutrinos are produced in the core of the Sun by nuclear reactions in which hydrogen is transformed into helium. The dominant sequence of reactions is the so-called  $pp$  chain [1,2], which is responsible for most of the solar luminosity, while approximately 1% of the solar energy is produced by the so-called carbon-nitrogen-oxygen (CNO) cycle. Even though the CNO cycle plays only a marginal role in the solar fusion mechanisms, it is expected to take over the luminosity budget for main sequence stars more massive, older, and hotter than the Sun [3]. Solar neutrinos have proven to be a powerful tool to study the solar core [4–7] and, at the same time, have been of paramount importance in shedding light on the neutrino oscillation phenomenon [8–13].

One important open question concerning solar physics regards the metallicity of the Sun, that is, the abundance of elements with  $Z > 2$ . In fact, different analyses of

\*Present affiliation: Max-Planck-Institut für Kernphysik, 69117 Heidelberg, Germany.

†Present affiliation: IHEP Institute of High Energy Physics, 100049 Beijing, People's Republic of China.

‡Present affiliation: INFN Laboratori Nazionali del Gran Sasso, 67010 Assergi (AQ), Italy.

§Present affiliation: Dipartimento di Fisica, Università degli Studi e INFN Milano-Bicocca, 20126 Milano, Italy.

||Present affiliation: Department of Physics and Astronomy, University of California, Irvine, California, USA.

¶Present affiliation: GSI Helmholtzzentrum für Schwerionenforschung GmbH, 64291 Darmstadt, Germany.

\*\*Present affiliation: Istituto Superiore per la Protezione e la Ricerca Ambientale, 00144 Roma, Italy.

*Published by the American Physical Society under the terms of the Creative Commons Attribution 4.0 International license. Further distribution of this work must maintain attribution to the author(s) and the published article's title, journal citation, and DOI. Funded by SCOAP<sup>3</sup>.*

spectroscopic data yield significantly different metallicity results that can be grouped in two classes: the so-called high-metallicity (HZ) [14,15] and low-metallicity (LZ) [16–18] models. The solar neutrino fluxes, in particular, that from the CNO cycle reactions, can address this issue. Indeed, the SSM predictions of the CNO neutrino flux depend on the solar metallicity directly, via the abundances of C and N in the solar core, and indirectly, via its effect on the solar opacity and temperature profile.

Borexino delivered the first direct experimental proof of the existence of the CNO cycle in the Sun with a significance of  $\sim 7\sigma$ , also providing a slight preference toward high-metallicity models [4,19]. This result was obtained with a multivariate analysis of the energy and radial distributions of selected events. To disentangle the CNO signal from the background, the multivariate fit requires an independent external constraint on the *pep* neutrino rate and on the  $^{210}\text{Bi}$  rate; the latter is obtained by tagging  $^{210}\text{Bi}$ – $^{210}\text{Po}$  coincidences in a temperature stabilized, layered scintillator fluid (see [4,19] for more details). For this reason, the CNO measurement has been performed only on approximately one-third of the Borexino data, the so-called Phase-III.

In this paper, we present new results on CNO neutrinos obtained exploiting the “correlated and integrated directionality” (CID) technique, which uses the directional information encoded in the Cherenkov light emitted alongside the scintillation, to separate the solar signal from nonsolar backgrounds. Borexino demonstrated the viability of this technique using  $^7\text{Be}$  solar neutrinos [20,21]. Here, we apply the CID technique to the CNO analysis, obtaining two important results: we show that we can extract the evidence of solar CNO neutrinos on the entire Borexino dataset following an alternative approach with respect to the standard multivariate analysis and, consequently, without the help of the  $^{210}\text{Bi}$  constraint; we also show that by combining the information coming from the directionality with the standard multivariate analysis performed on Phase-III data, we obtain an improved measurement of the CNO neutrino interaction rate.

The paper is structured as follows. Section II describes the Borexino detector and summarizes the event reconstruction techniques. The CID analysis for the CNO neutrino measurement is illustrated in Sec. III, outlining the methods, reporting the results, and detailing the main sources of systematic uncertainties. Finally, in Sec. IV we show our best result on CNO neutrinos obtained combining the CID and the standard multivariate analysis.

## II. THE BOREXINO EXPERIMENT

Borexino was a liquid scintillator (LS) neutrino detector [22] that ran until October 2021 with unprecedented radiopurity levels [5,23], a necessary feature of its solar neutrino measurements. The detector was located deep underground at the Laboratori Nazionali del Gran Sasso (LNGS) in Italy, with about 3800 m water equivalent rock

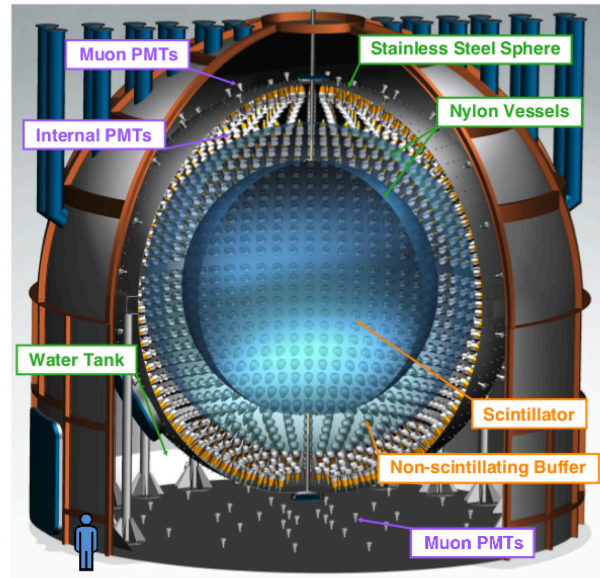


FIG. 1. Scheme of the Borexino detector.

shielding suppressing the cosmic muon flux by a factor of  $\sim 10^6$ .

The detector layout is schematically shown in Fig. 1. The stainless steel sphere (SSS) with a 6.85 m radius supported 2212 8-inch photomultiplier tubes (PMTs) and contained 280 tonnes of pseudocumene (1, 2, 4-trimethylbenzene, PC) doped with 1.5% of PPO (2, 5-diphenyloxazole) wavelength shifter, confined in a nylon inner vessel of 4.25 m radius. The density of the scintillator was  $(0.878 \pm 0.004) \text{ g cm}^{-3}$  with the electron density of  $(3.307 \pm 0.015) \times 10^{31} e^-/100 \text{ tonnes}$ . The PC-based buffer liquid in the region between the SSS and IV shielded the LS from external  $\gamma$  radiation and neutrons. The nylon outer vessel, which separated the buffer in two subvolumes, prevented the inward diffusion of  $^{222}\text{Rn}$ . The SSS itself is submerged in a domed, cylindrical tank filled with  $\sim 1$  kton of ultra-pure water, equipped with 208 PMTs. The water tank provided shielding against external backgrounds and also served as an active Cherenkov veto for residual cosmic muons passing through the detector.

Borexino detected solar neutrinos via their elastic scattering on electrons of the LS, a process sensitive, with different probability, to all neutrino flavors. Electrons, and charged particles in general, deposit their energy in the LS, excite its molecules, and the resulting scintillation light is emitted isotropically. Using  $n \approx 1.55$  as scintillator index of refraction at 400 nm wavelength, subdominant but directional Cherenkov light is emitted when the electron kinetic energy exceeds 0.165 MeV. Cherenkov light is emitted over picosecond timescale, while the fastest scintillation light component from the LS has an emission time constant at the nanosecond level. The fraction of light emitted as Cherenkov photons in Borexino was less than 0.5% for 1 MeV recoiling electrons.

The effective total light yield was  $\sim 500$  photoelectrons per MeV of electron equivalent deposited energy, normalized to 2000 PMTs [23]. The energy scale is intrinsically nonlinear due to ionization quenching and the emission of Cherenkov radiation. The GEANT4 based Monte Carlo (MC) software [24] simulates all relevant physics processes. It is tuned using the data obtained during calibration campaigns with radioactive sources [25]. Distinct energy estimators have been defined, based on different ways of counting the number of detected photons [20,23]. The position reconstruction of each event is performed by using the time-of-flight corrected detection time of photons on hit PMTs [23]. Particle identification is also possible in Borexino [23], in particular,  $\alpha/\beta$  discrimination [4], by exploiting different scintillation light emission time profiles.

The Borexino data-taking period is divided into three phases: Phase-I (May 2007–May 2010), Phase-II (December 2011–May 2016), and Phase-III (July 2016–October 2021). Phase-II started after the detector calibration [25] and an additional purification of the LS, which enabled a comprehensive measurement of the  $pp$  chain solar neutrinos [5]. Phase-III is characterized by a thermally stable detector with greatly suppressed seasonal convective currents. This condition has made it possible to extract an upper limit constraint on the  $^{210}\text{Bi}$  contamination in the LS, and thus, to provide the first direct observation of solar CNO neutrinos [4].

### III. CORRELATED AND INTEGRATED DIRECTIONALITY FOR CNO

Cherenkov photons emitted by the electrons scattered in neutrino interactions retain information about the original direction of the incident neutrino. Typically, in water Cherenkov neutrino detectors, this information is accessed through an event-by-event direction reconstruction, as demonstrated by the measurements of  $^8\text{B}$  neutrinos, at energies larger than 3.5 MeV [7,26]. Instead, the Borexino experiment has provided a proof of principle for the use of this Cherenkov hit information in a LS detector and at neutrino energies below 1 MeV through the so-called CID technique. A detailed explanation of the method can be found in [20,21].

The CID method discriminates the signal originating in the Sun—due to solar neutrinos—from the background. Cherenkov light is subdominant in Borexino, but it is emitted almost instantaneously with respect to the slower scintillation light. Consequently, directional information is contained in the first hits of an event (after correcting for the time of flight of each photon). The CID analysis is based on the  $\cos \alpha$  observable: For a given PMT hit in an event,  $\alpha$  is the aperture angle between the Sun and the hit PMT at the reconstructed position of the event (see also Fig. 3 in [20]). For background events, the  $\cos \alpha$  distribution is nearly uniform regardless of which hit is considered. For solar neutrino events, the  $\cos \alpha$  distribution is flat for scintillation photons, which are emitted isotropically, but has a characteristic nonflat distribution peaked at  $\cos \alpha \sim 0.7$  for

Cherenkov hits correlated with the position of the Sun. Since we cannot distinguish Cherenkov and scintillation photons, in our previous work [21], we have used only the first and second hits of each event, which have the largest probability of being Cherenkov hits. In the new analysis presented in this paper, we fully exploit the directional information contained in the first several hits. This choice is supported by Monte Carlo simulations and sensitivity studies as discussed in Sec. III B.

The solar neutrino signal is obtained by fitting the  $\cos \alpha$  distributions of the selected first several hits, as a sum of signal and backgrounds contributions. The expected  $\cos \alpha$  distributions for signal and background are obtained from Monte Carlo simulations. As in Ref. [20], for each selected data event, we simulate 200 MC events of solar neutrinos (represented by  $^7\text{Be}$  or  $pep$  according to RoI, see below) and the same amount of the background events (represented by  $^{210}\text{Bi}$ ). These events are simulated with the same astronomical time as the data event and with the position smeared around the reconstructed vertex. From the fit, we then obtain the total number of solar neutrinos  $N_\nu$  detected in the RoI. The fit also includes two nuisance parameters. The effective Cherenkov group velocity correction  $gv_{\text{ch}}$  nuisance parameter accounts for small differences in the relative hit time distribution between scintillation and Cherenkov hits in data relative to the MC. The scintillation and Cherenkov photons have a different wavelength distribution (see Fig. 6 in [20]). Given the wavelength dependent refractive index of the LS, this means that they have different average group velocities  $\bar{v}_g$ . For the CID analysis, only the difference  $\Delta \bar{v}_g = \bar{v}_g(\text{Cherenkov}) - \bar{v}_g(\text{scintillation})$  is of importance, and this value can be different between data and MC,  $\Delta \bar{v}_g(\text{Data}) \neq \Delta \bar{v}_g(\text{MC})$ . The  $gv_{\text{ch}}$  is now an effective correction of the Cherenkov group velocity, such that  $\Delta \bar{v}_g(\text{Data}) = \Delta \bar{v}_g(\text{MC}(gv_{\text{ch}}))$  is fulfilled. It is implemented in MC on the PMT hit time:

$$t_{\text{new}}^{\text{ToF}} = t_{\text{old}}^{\text{ToF}} - gv_{\text{ch}} \cdot L_{\text{true}}, \quad (1)$$

where  $t_{\text{new}}^{\text{ToF}}$ ,  $t_{\text{old}}^{\text{ToF}}$  is the modified hit time of the Cherenkov photons and is their normal MC hit time, respectively, and  $L_{\text{true}}$  is the MC track length of the photon. The second parameter is the event position mis-reconstruction in the initial electron direction  $\Delta r_{\text{dir}}$ , an indirect effect of the Cherenkov hits, where the reconstructed position is slightly biased toward early hit PMTs of the corresponding event. Here,  $\Delta r_{\text{dir}}$  is a free parameter of the fit, while  $gv_{\text{ch}}$  is obtained independently and is constrained in the fit.

Compared to the previous proof-of-principle analysis [20,21], the current CID analysis has been improved in a variety of ways. The full detector live time can be used now thanks to a novel  $gv_{\text{ch}}$  correction calibration. In the previous publication,  $gv_{\text{ch}}$  has been obtained using  $^{40}\text{K}$   $\gamma$  calibration data (see [20]). In this work, instead, we calibrate  $gv_{\text{ch}}$  by exploiting the  $^7\text{Be}$  solar neutrino events,

which allows us to extend the analysis to the full Borexino dataset, as explained in Sec. III A. Additionally, indirect Cherenkov information from the systematic influence on the vertex reconstruction and consequently on the  $\cos\alpha$  distribution was exploited by the inclusion in the analysis of later hits with negligible contribution of Cherenkov photons; see Sec. III B. Technical details of the CID fitting procedure can be found in Sec. III C, while different systematic effects are discussed in Sec. III D. The final CID results regarding the CNO measurement are reported in Sec. III E.

### A. CID strategy for the CNO measurement with the full dataset

In the previous Borexino works [20,21], the calibration of the Cherenkov light group velocity  $g_{\text{ch}}$  has been performed using  $\gamma$  sources deployed during the Borexino calibration campaign in 2009 [20]. The solar neutrino analysis was performed on the Phase-I dataset, which has been taken close in time to the source calibration of the detector [25]. The  $g_{\text{ch}}$  found in this way was used to obtain the first measurement of  ${}^7\text{Be}$  solar neutrinos with the CID method [21]. For the CID measurement of CNO in this paper, the entire Borexino dataset is used (from 2007 until 2021). Since the sub-nanosecond stability of the detector time response cannot be guaranteed for long periods, and no more calibrations have been performed after 2009, we developed a method to calibrate  $g_{\text{ch}}$  on the  ${}^7\text{Be}$  shoulder data. This is done by using the same RoI as in [20,21] (here, called  $\text{RoI}_{\text{gvc}}$  electron equivalent energy range of  $0.5 \text{ MeV} \lesssim T_e \lesssim 0.8 \text{ MeV}$ ) and performing the CID analysis where the  ${}^7\text{Be}$  is constrained to the average of low metallicity and high metallicity Standard Model predictions ( $43.7 \pm 2.5 \text{ cpd}/100 \text{ t}$  and  $47.9 \pm 2.8 \text{ cpd}/100 \text{ t}$  for LZ-SSM and HZ-SSM, respectively) [2]. The  $g_{\text{ch}}$  correction extracted in this way is then used in the CID analysis of the  $\text{RoI}_{\text{CNO}}$ , in which the CNO contribution is maximized, and which is fully independent from  $\text{RoI}_{\text{gvc}}$ . This step has been found to be justified according to MC studies, as the wavelength distribution of the detected Cherenkov photons produced by electrons from  $\text{RoI}_{\text{gvc}}$  and  $\text{RoI}_{\text{CNO}}$  is the same. With this new strategy, the Cherenkov light  $g_{\text{ch}}$  can be calibrated on the same data-taking period as the one used for the CNO analysis. Two analyses have been performed in parallel for Phase-I (May 2007 to May 2010, 740.7 days) and Phase-II + III (December 2011 to October 2021, 2888.0 days). The  $g_{\text{ch}}$  correction obtained for Phase-I can be compared to the one previously obtained from the  ${}^{40}\text{K}$   $\gamma$  source [20]. Additionally, the analyses of the two independent datasets allows for the investigation of any variation of the detector response over time. The  $\text{RoI}_{\text{gvc}}$  and the  $\text{RoI}_{\text{CNO}}$  are shown for the Phase-II + III dataset in Fig. 2 for illustrative purposes. The results on  $g_{\text{ch}}$  are provided in Sec. III E 1.

In the final analysis, the threefold-coincidence algorithm [4] is applied to the  $\text{RoI}_{\text{CNO}}$  to suppress the cosmogenic  ${}^{11}\text{C}$

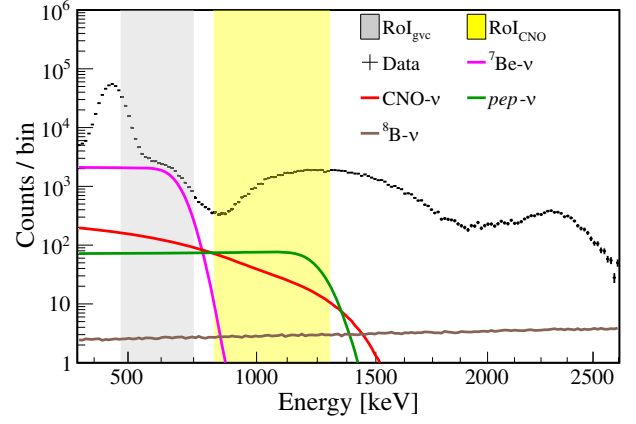


FIG. 2. Illustration of the two RoIs used in the analysis on the energy spectrum of the Phase-II + III data in a fiducial volume of 2.95 m radius. Monte Carlo PDFs of different solar neutrino components are scaled to high-metallicity SSM prediction [2]. The gray band shows the  ${}^7\text{Be}$ - $\nu$  edge region used for the estimation of  $g_{\text{ch}}$  correction ( $\text{RoI}_{\text{gvc}}$ ), while the CNO region used to measure the CNO- $\nu$  rate is shown in the yellow band ( $\text{RoI}_{\text{CNO}}$ ).

background, preserving the exposure with a signal survival fraction of  $55.77\% \pm 0.02\%$  for Phase-I and  $63.97\% \pm 0.02\%$  for Phase-II + III. The radial ( $R_{\text{FV}}$ ) and  $T_e$  energy cuts of  $\text{RoI}_{\text{CNO}}$  were optimized considering the expected number of solar neutrinos over the statistical uncertainty of the total number of events. For the Phase-I dataset, the optimized cuts are  $R_{\text{FV}} < 3.05 \text{ m}$  and  $0.85 \text{ MeV} < T_e < 1.3 \text{ MeV}$ . Regarding Phase-II + III, the optimized cuts are instead  $R_{\text{FV}} < 2.95 \text{ m}$  and  $0.85 \text{ MeV} < T_e < 1.29 \text{ MeV}$ . In addition, all other cuts including the muon veto and data quality cuts have been applied as in Refs. [4,19]. The overall exposures for the CID CNO analysis are  $740.7 \text{ days} \times 104.3 \text{ tonnes} \times 55.77\%$  for Phase-I and  $2888.0 \text{ days} \times 94.4 \text{ tonnes} \times 63.97\%$  for Phase-II + III. The total exposure of Phase-II + III ( $477.81 \text{ years} \times \text{tonnes}$ ) is about four times larger than that of Phase-I ( $118.04 \text{ years} \times \text{tonnes}$ ).

### B. $N^{\text{th}}$ -hit analysis approach

As mentioned above, the CID analysis is performed on the first several early hits of ToF corrected hit times from each event in the RoI. In this subsection, we describe the optimization of the number of hits from each event to be used in the CID analysis. The procedure is based on the comparison of the MC-produced  $\cos\alpha$  distributions of signal and background.

First, PMT hits of each individual event are sorted according to their ToF-corrected hit times and are labeled in this order as “ $N^{\text{th}}$  hit,” with  $N = 1, 2, \dots$  up to the total number of hits. Second, the  $\cos\alpha$  distributions are constructed for each  $N^{\text{th}}$  hit for both the signal and background MC. Third, for each  $N^{\text{th}}$ -hit  $\cos\alpha$  distribution, a number of 10,000 toy MC samples are simulated with the

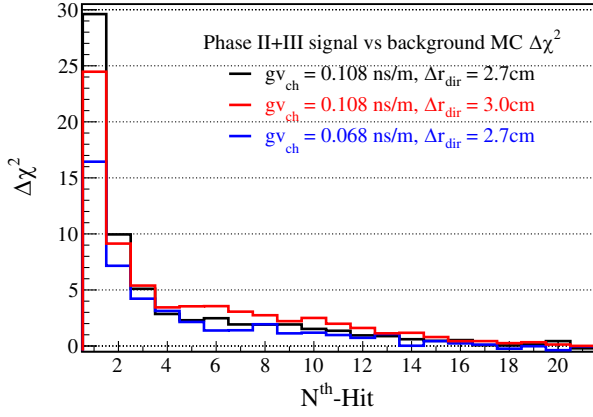


FIG. 3.  $\Delta\chi^2$  between the Phase-II + III RoI<sub>CNO</sub> neutrino signal and background MC  $\cos\alpha$  distributions for different selections of nuisance parameters.  $\Delta r_{\text{dir}} = 2.7$  cm corresponds to the nominal value observed in the neutrino MC.

number of events observed as in the real data. Next, we perform a direct signal to background comparison, based on a standard  $\chi^2$ -test. Figure 3 shows the resulting  $\Delta\chi^2$  for Phase-II + III in the RoI<sub>CNO</sub> averaged over the 10,000 toy datasets as a function of  $N^{\text{th}}$  hit. A larger average  $\Delta\chi^2$  corresponds to a greater difference between the MC signal and background and thus a larger expected sensitivity for the CID fit, independent of the true signal to background ratio. While only the earliest  $\sim 4$   $N^{\text{th}}$  hits have a relevant, *direct* contribution of Cherenkov hits to the  $\cos\alpha$  distribution of the neutrino signal, later  $N^{\text{th}}$  hits also contribute to the CID sensitivity due to the *indirect* Cherenkov influence on  $\Delta r_{\text{dir}}$ .

The impact of the  $\Delta r_{\text{dir}}$  parameter on the neutrino  $\cos\alpha$  distribution is schematically illustrated in Fig. 9 in [20]. This  $\Delta r_{\text{dir}}$  parameter arises due to the position reconstruction algorithm of Borexino [25], where early PMT hits tend to pull the reconstructed position toward them. Because Cherenkov photons are, on average, emitted earlier than scintillation photons and because the Cherenkov direction of the neutrino signal is correlated to the assumed solar direction, this small position reconstruction bias has a visible impact on the  $\cos\alpha$  distribution of the signal.

A possible impact of the  $g_{\text{vch}}$  and  $\Delta r_{\text{dir}}$  nuisance parameters on the  $N^{\text{th}}$ -hit selection has been investigated and is presented in Fig. 3. The first hits of the events provide the largest  $\Delta\chi^2$  values thanks to the direct Cherenkov light. A decrease of  $g_{\text{vch}}$  is decreasing the group velocity of Cherenkov photons and thus their contribution at early hits. The impact of  $\Delta r_{\text{dir}}$  can be seen for  $N^{\text{th}}$  hit  $> 4$ , where the contribution of direct Cherenkov hits becomes negligible relative to the scintillation hits, but the signal and background MC  $\cos\alpha$  histograms are still different from each other ( $\Delta\chi^2 > 0$ ).

In conclusion, the early hits selection for the CID analysis in both RoI<sub>gvc</sub> and RoI<sub>CNO</sub> is then performed from the first hit up to the  $N^{\text{th}}$  hit(max) = 15, 17 for

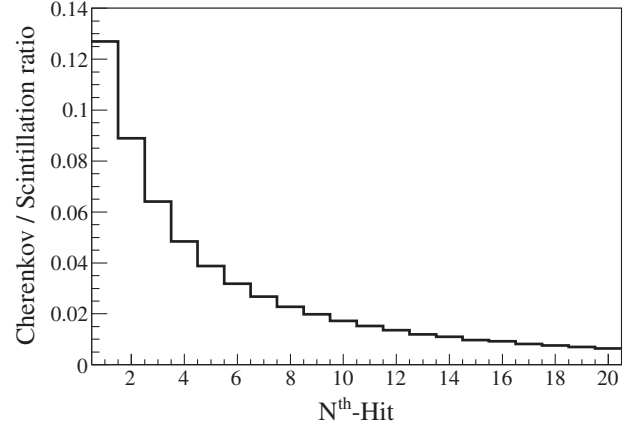


FIG. 4. Cherenkov-to-scintillation PMT hit ratio as a function of the time-of-flight sorted  $N^{\text{th}}$  hits for the *pep* neutrino Monte Carlo of Phase II + III in the RoI<sub>CNO</sub> (0.85–1.3 MeV).

Phase-I and Phase-II + III, respectively. This is an optimization where all direct and indirect Cherenkov information is used, while at the same time, this selection keeps the contribution from delayed scintillation photons, undergoing various optical process during the propagation through the detector, relatively small.

The Cherenkov-to-scintillation photon ratio as a function of  $N^{\text{th}}$  hit has also been checked explicitly, as is shown in Fig. 4 for RoI<sub>CNO</sub>. As expected, it can be seen that the early  $N^{\text{th}}$  hits benefit from the largest Cherenkov-to-scintillation ratio of  $\sim 13\%$  for the first hit. The overall total Cherenkov-to-scintillation ratio is small and found to be 0.475% in the MC.

### C. CID fit procedure

The fitting strategy follows the procedure developed in our previous CID analysis [20]. The data  $\cos\alpha$  distributions from the selected RoI, constructed for each  $N^{\text{th}}$  hit from the first up to the  $N^{\text{th}}$  hit(max), are fitted simultaneously with the MC produced, expected  $\cos\alpha$  distributions of the neutrino signal and background, where the signal  $\cos\alpha$  distribution depends on  $g_{\text{vch}}$  and  $\Delta r_{\text{dir}}$ . The nuisance parameter  $\Delta r_{\text{dir}}$  cannot be calibrated in Borexino and is left free to vary without a dedicated pull term. The number of  $\cos\alpha$  histogram bins used in the analyses is  $I = 60$  for all energy regions and phases, as values of  $I < 30$  reduce the expected CID sensitivity.

#### 1. Fit in the RoI<sub>gvc</sub>

The CID analysis in RoI<sub>gvc</sub> used for the  $g_{\text{vch}}$  calibration is based on the  $\chi^2$  test:

$$\begin{aligned} \chi_{g_{\text{vch}}}^2(N_\nu, g_{\text{vch}}, \Delta r_{\text{dir}}) &= \sum_{n=1}^{N^{\text{th}} \text{ hit(max)}} \sum_{i=1}^I \left( \frac{(norm \cdot M_i^n - D_i^n)^2}{norm \cdot M_i^n + norm^2 \cdot M_i^n} \right) - 2 \ln(P(N_\nu)), \end{aligned} \quad (2)$$

where  $D_i^n$  and  $M_i^n$  are the numbers of  $\cos\alpha$  histogram entries at bin  $i$  for a given  $N^{\text{th}}$ -hit  $n$ , for data and MC, respectively. The term *norm* is the scaling factor between the MC and the data event statistics and the term “ $norm^2 \cdot M_i^n$ ” in the denominator takes into account the finite statistics of MC. The explicit dependence of the fit on  $N_\nu$ ,  $gv_{\text{ch}}$ , and  $\Delta r_{\text{dir}}$  can be expressed by decomposing the MC contribution to the one from the signal  $S$  and the background  $B$ :

$$M_i^n = \frac{N_\nu}{N_{\text{data}}} \cdot M_{S,i}^n(\Delta r_{\text{dir}}, gv_{\text{ch}}) + \left(1 - \frac{N_\nu}{N_{\text{data}}}\right) \cdot M_{B,i}^n. \quad (3)$$

The number of neutrino events  $N_\nu$  and  $\Delta r_{\text{dir}}$  are treated as nuisance parameters to produce the  $\chi^2(gv_{\text{ch}})$  profile, where  $N_\nu$  is constrained by the SSM expectation. For this, the neutrino prior probability distribution  $P(N_\nu)$  is given by the sum of the Gaussian probability distributions with mean  $(N_{\text{Be}}, N_{\text{pep}})$  and uncertainty  $(\sigma_{\text{Be}}, \sigma_{\text{pep}})$  from the high-metallicity (HZ) SSM and low-metallicity (LZ) SSM [2] predictions on the number of  ${}^7\text{Be} + \text{pep}-\nu$  in  ${}^7\text{Be}-\nu$  shoulder region, which is then convoluted with a uniform distribution of  $N_{\text{CNO}}^{\text{HZ}}$  between zero and the HZ-SSM CNO expectation,  $5\sigma_{\text{CNO}}^{\text{HZ}}$ :

$$\begin{aligned} P(N_\nu) &\propto ((\varphi_{\text{HZ}} + \varphi_{\text{LZ}}) * f)(N_\nu) \\ \varphi(N_\nu) &= \exp\left(-\frac{1}{2} \frac{(N_\nu - (N_{\text{Be}} + N_{\text{pep}}))^2}{\sigma_{\text{Be}}^2 + \sigma_{\text{pep}}^2}\right) \\ f(N_\nu) &= \begin{cases} 1 & \text{if } 0 \leq N_\nu \leq N_{\text{CNO}}^{\text{HZ}} + 5\sigma_{\text{CNO}}^{\text{HZ}} \\ 0 & \text{otherwise.} \end{cases} \end{aligned} \quad (4)$$

In this way, by leaving CNO reasonably free to vary, we avoid a potential correlation of the  $gv_{\text{ch}}$  calibration and the subsequent measurement of the CNO- $\nu$  rate using this  $gv_{\text{ch}}$  constraint.

## 2. Fit in the $\text{RoI}_{\text{CNO}}$

The  $\chi^2$  test for the measurement of number of solar neutrinos ( $N_\nu$ ) in  $\text{RoI}_{\text{CNO}}$  is

$$\begin{aligned} \chi_\nu^2(N_\nu, gv_{\text{ch}}, \Delta r_{\text{dir}}) &= \sum_{n=1}^{N^{\text{th}} \text{ hit}(\text{max})} \sum_{i=1}^I \left( \frac{(norm \cdot M_i^n - D_i^n)^2}{norm \cdot M_i^n + norm^2 \cdot M_i^n} \right) \\ &+ \Delta\chi_{gv_{\text{ch}}}^2(gv_{\text{ch}}), \end{aligned} \quad (5)$$

using  $gv_{\text{ch}}$  and  $\Delta r_{\text{dir}}$  as nuisance parameters. The  $gv_{\text{ch}}$  parameter is now constrained by the previous calibration in  $\text{RoI}_{\text{gvc}}$  through the pull term  $\Delta\chi_{gv_{\text{ch}}}^2(gv_{\text{ch}})$ , defined as the following:

$$\Delta\chi_{gv_{\text{ch}}}^2(gv_{\text{ch}}) = \frac{(gv_{\text{ch}} - gv_{\text{ch}}^{\text{result}})^2}{\sigma(gv_{\text{ch}}^{\text{result}})^2}, \quad (6)$$

where  $gv_{\text{ch}}^{\text{result}}$  and  $\sigma(gv_{\text{ch}}^{\text{result}})$  represents the results on  $gv_{\text{ch}}$  parameter obtained in  $\text{RoI}_{\text{gvc}}$  and its  $1\sigma$  error.

## D. Systematic uncertainties

In this work, we have performed a detailed evaluation of the systematic uncertainties. The quantitative evaluation of the systematic uncertainties on the CID analysis results is given in Sec. III E.

It has been found that the choice of  $N^{\text{th}}$  hit(max) and the histogram binning do not introduce any systematic uncertainty. Backgrounds different than  ${}^{210}\text{Bi}$  also contribute in the analyzed energy intervals but have been found to be indistinguishable in the CID analysis and do not contribute to the systematic uncertainty budget. Even if the external  $\gamma$  events are not uniformly distributed in the FV, due to their attenuation in the LS, the difference in the  $\cos\alpha$  distribution between these events and uniform background events is found to be safely negligible, given the statistics of the data.

The following effects have an impact on the final results:

*PMT selection:* Some PMTs feature an intrinsic misbehavior of their hit time distribution, if compared to all other PMTs. They are identified through a fit of their individual hit time distribution, given by an enriched sample of  ${}^{11}\text{C}$  events. In addition, a small number of PMTs feature inconsistency between the data and MC in the relative contribution to the first hits. The systematic effect of the PMT selection has been evaluated by varying the selection of usable PMT.

*Relative PMT hit time correction:* It has been found by analyzing an enriched sample of  ${}^{11}\text{C}$  events that the data PMTs have a small relative time offset between each other with an average value of 0.3 ns. This time offset has been measured with an uncertainty of up to  $\pm 0.1$  ns. It is reasonable to correct this relative offset in data, as it does not exist in MC. This makes it also necessary to propagate the uncertainty of the PMT time correction through the entire analysis chain, which introduces a systematic uncertainty.

*Influence of low number of signal events:* As described above, signal and background MC are produced on an event-by-event basis. This could introduce an additional systematic uncertainty through the particular choice of the event positions and neutrino directions used for the production of the signal MC. The reason for this is the geometric effect that gives rise to the nonflat background distribution, due to the distribution of live PMTs and solar directions at the latitude of Borexino. It is unknown which subset of the data events corresponds to the true neutrino events, and it has been found that a sufficiently small number of neutrino events can produce subsets of the corresponding signal MC  $\cos\alpha$  distributions that are

noticeably different from each other. Therefore, this systematic uncertainty is estimated by producing a large number of the signal MC  $\cos\alpha$  distributions corresponding to a random selection of the expected number of signal events from data in each phase. The data is then analyzed again with these reduced signal MC  $\cos\alpha$  histograms. This effect is found to have a contribution to the systematic uncertainty only in the  $\text{RoI}_{\text{CNO}}$  of Phase-I.

*CNO- $\nu$  and  $pep$ - $\nu$   $\cos\alpha$  distributions:* The CNO- $\nu$  and  $pep$ - $\nu$  events show a significantly different energy distribution in the selected RoI. The expected Cherenkov to scintillation hits ratio for  $pep$ - $\nu$  events (0.475%) is higher than for CNO events (0.469%) due to their different energy distribution in  $\text{RoI}_{\text{CNO}}$ . Moreover, the angular distribution of recoiled electrons by CNO- $\nu$  and  $pep$ - $\nu$  is also different due to its dependence on energy distributions of the neutrino and recoiled electron. The final fit on the number of solar neutrinos is performed with the  $pep$ - $\nu$  MC and the systematic uncertainty is estimated by performing the CID analysis again with the CNO- $\nu$  MC. The absolute difference between the two analyses is used conservatively as the systematic uncertainty. This systematic is negligible for the  $g_{\text{vch}}$  calibration, as CNO +  $pep$  neutrinos are subdominant to the  ${}^7\text{Be}$  neutrinos.

*Constraint on non-CNO neutrinos:* The CID analysis is only sensitive to the measurement of the total number of solar neutrinos  $N_\nu$  and cannot differentiate between different solar neutrino species. Therefore, a measurement of the number of CNO neutrinos depends on the subtraction of the non-CNO neutrinos from  $N_\nu$  obtained in the  $\text{RoI}_{\text{CNO}}$ . The number of  $pep$  neutrinos is constrained by the SSM predictions [2], while  ${}^8\text{B}$  is constrained using the high precision flux measurement of Super-Kamiokande [6].

*Exposure:* In this category, we cover systematic uncertainties on the determination of the fiducial mass and on the fraction of solar neutrinos in the RoI. These uncertainties are estimated using toy-MC studies, based on the results of the calibration campaign [25], on the performance of the position reconstruction, and on the uncertainty on the energy scale described in [4], respectively. The uncertainty on the fiducial mass includes also the uncertainty on the scintillator density. Additionally, in the  $g_{\text{vch}}$  calibration using the constraint on the expected number of all solar neutrino events, we consider also the uncertainty on  $\alpha/\beta$  discrimination applied to suppress  ${}^{210}\text{Po}$   $\alpha$  decays in the  $\text{RoI}_{\text{gvc}}$ .

## E. Results of the CID analysis

### 1. Effective $g_{\text{vch}}$ calibration on the ${}^7\text{Be}$ edge

The effective calibration of the Cherenkov light as a results of the CID analysis on the  ${}^7\text{Be}$  edge, using Eq. (2), is

TABLE I. Systematic uncertainties of the  $g_{\text{vch}}$  measurement in the  $\text{RoI}_{\text{gvc}}$ , relative to the best fit value.

Source of $g_{\text{vch}}$ uncertainty	Phase-I (%)	Phase-II + III (%)
PMT selection	2.1	1.6
PMT time corrections	3.7	2.1
MLP event selection	1.0	1.0
Fiducial mass	$\begin{pmatrix} +0.2 \\ -1.2 \end{pmatrix}$	$\begin{pmatrix} +0.2 \\ -1.2 \end{pmatrix}$
Fraction of neutrinos in RoI	1.3	0.9

$g_{\text{vch}} = (0.140 \pm 0.029) \text{ ns m}^{-1}$  for Phase-I and  $g_{\text{vch}} = (0.089 \pm 0.019) \text{ ns m}^{-1}$  for Phase-II + III, including the systematic uncertainties summarized in Table I. The compatibility between the data and the MC model, illustrated in Fig. 5, is good with  $\chi^2/\text{ndf} = 874.9/897$ ,  $p$  value = 0.70 for Phase-I and  $\chi^2/\text{ndf} = 1036.2/1017$ ,  $p$  value = 0.33 for Phase-II + III. The  $\chi^2/\text{ndf}$  and  $p$  values have also been investigated for the individual  $N^{\text{th}}$ -hits  $\cos\alpha$  histograms, with different binning choices to investigate the fit performance. For all cases, the best fit MC model  $\cos\alpha$  distribution is always in agreement with the data. Figure 5 shows an illustration of the best fit results (red) relative to a pure background hypothesis (blue). For early hits, direct Cherenkov light causes the peak seen for  $\cos\alpha > 0$ , and the influence of  $\Delta r_{\text{dir}}$  induces the negative slope for  $\cos\alpha < 0$ . For later  $N^{\text{th}}$  hits, the Cherenkov peak washes away, but the indirect impact of the Cherenkov hits on the position reconstruction bias  $\Delta r_{\text{dir}}$  makes it still possible to distinguish between the neutrino signal and the background. The nonflat background  $\cos\alpha$  distribution originates from the live PMT nonisotropic distribution relative to the position distribution of the Sun around Borexino. These  $g_{\text{vch}}$  values for Phase-I and Phase-II + III differ by less than  $1.5\sigma$  and both are in agreement with the previous calibration performed at the end of Phase-I using a  ${}^{40}\text{K}$   $\gamma$  source:  $g_{\text{vch}} = (0.108 \pm 0.039) \text{ ns m}^{-1}$  (Fig. 13 in [20]).

### 2. CNO measurement with CID

This section describes the results of the measurement of CNO solar neutrinos with CID using the full Borexino live time from May 2007 to October 2021. The  $g_{\text{vch}}$  values presented in Sec. III E 1 are used as independent pull terms in Eq. (5) for the fit in  $\text{RoI}_{\text{CNO}}$  of their respective phases. This takes into account the potential systematic differences of the detector response between Phase-I and Phase-II + III. The resulting number of solar neutrino events  $N_\nu$  in the  $\text{RoI}_{\text{CNO}}$  can be converted into the number of CNO neutrinos detected in the same energy region after constraining the contributions from  $pep$  and  ${}^8\text{B}$  neutrinos, but without any *a priori* knowledge of the backgrounds. This number of CNO events can be further transformed into the measurement of the CNO- $\nu$  interaction rate in Borexino and the CNO flux at Earth.

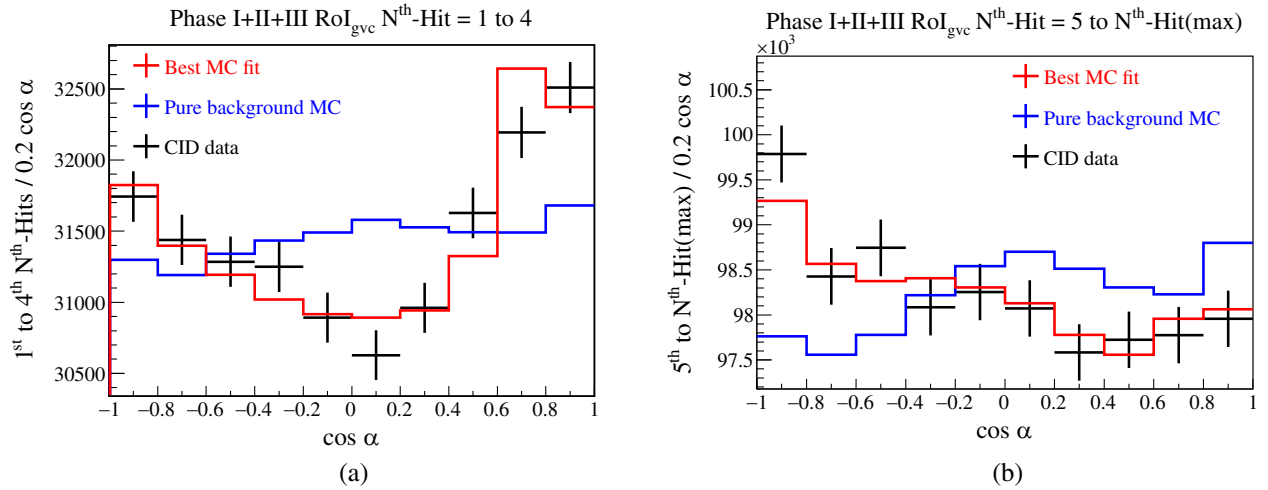


FIG. 5. The CID data (black) and the best fit results (red) for the measurement of the  $g_{v_{ch}}$  parameter. While the analysis is done separately for Phase-I and Phase-II + III, here, the sum of Phase-I + II + III is shown for illustration purposes. There are in total  $7.86 \times 10^4$  events in the RoI<sub>gvc</sub>. The best fit for the constrained number of neutrino events is  $N_\nu = 5.00 \times 10^4$ , while the best fit values for the parameter of interest are  $g_{v_{ch}} = 0.140 \text{ ns m}^{-1}$  for Phase-I and  $g_{v_{ch}} = 0.089 \text{ ns m}^{-1}$  for Phase-II + III. For comparison, the background MC (blue) scaled to the same total number of events is shown. (a) The sum of the first to fourth N<sup>th</sup>-hits  $\cos \alpha$  histograms shows the Cherenkov peak. (b) The sum of the fifth to the N<sup>th</sup>-hit(max)  $\cos \alpha$  histograms shows the effect the  $\Delta r_{dir}$  parameter on the later hits.

The best fit values for the number of solar neutrinos in RoI<sub>CNO</sub> are  $N_\nu = (6.9 + 2.4 - 2.2) \times 10^2$  (stat) for Phase-I and  $N_\nu = (28.2 + 5.2 - 4.9) \times 10^3$  (stat) for Phase-II + III without inclusion of any systematic uncertainties or corrections. The compatibility between the data and the MC model is good with  $\chi^2/\text{ndf} = 884.8/897$ ,  $p$  value = 0.61 for Phase-I and  $\chi^2/\text{ndf} = 1000.7/1017$ ,  $p$  value = 0.64 for Phase-II + III. The MC model is able to reproduce the data

$\cos \alpha$  distribution, which has also been investigated for the individual N<sup>th</sup>-hits  $\cos \alpha$  histograms.

Figure 6 illustrates the best fit results (red) relative to a pure background hypothesis (blue), in which the CID  $\cos \alpha$  histograms of data (black) are shown for the sum of Phase-I + Phase-II + III, as well as for the sum of the early first to fourth N<sup>th</sup> hits (top) and the sum of the later N<sup>th</sup> hits from the fifth to N<sup>th</sup> - hit(max) (bottom).

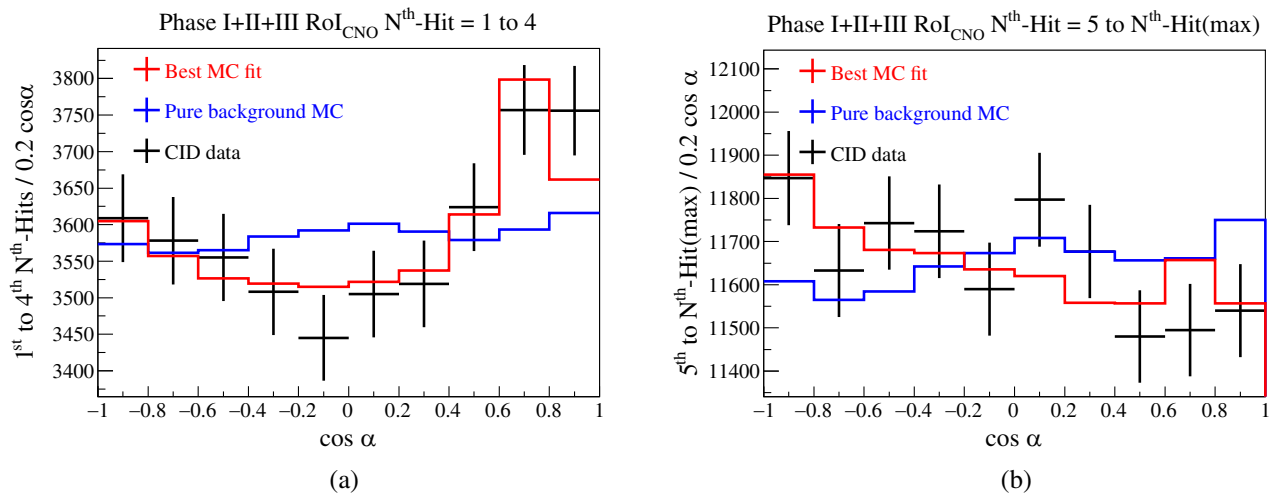


FIG. 6. Illustration of the CID data (black) and the best fit results (red) summed for the Phase-I + Phase-II + III with a total of 8964 events in the RoI<sub>CNO</sub>. The best fit of the total number of neutrino events is  $N_\nu = 3519$  without any systematic correction. For comparison, the background MC (blue) scaled to the same total number of events is shown. (a) The sum of the first to fourth N<sup>th</sup>-hits  $\cos \alpha$  histograms shows the Cherenkov peak. (b) The sum of the fifth to the N<sup>th</sup>-hit(max)  $\cos \alpha$  histograms shows the effect the  $\Delta r_{dir}$  parameter on these later hits.

The actual fit is performed on Phase-I and Phase-II + III independently. The same observations made for Fig. 5 hold also true for Fig. 6, where the early hits show the Cherenkov peak, and the later hits show the impact of  $\Delta r_{\text{dir}}$ .

*Fit response bias correction.* It has been found, through toy-MC analyses, that the number of solar neutrinos in  $\text{RoI}_{\text{CNO}}$  show a small systematic shift between the injected number of neutrinos and their corresponding best fit values. This fit response bias is induced by the two nuisance parameters ( $g_{\text{vch}}$ ,  $\Delta r_{\text{dir}}$ ), as they only impact the shape of the neutrino signal MC  $\cos \alpha$  distribution but not that of background. An increase of the best fit number of neutrino events increases the impact of the nuisance parameters on the MC  $\cos \alpha$  shape, which can be understood somewhat as an effective increase of the number of free parameters in the fit. Therefore, purely statistical fluctuations of the data  $\cos \alpha$  distribution can be better accommodated with a larger best fit value of the number of neutrino events, which results in the observed fit response bias. This effect depends on the true total number of neutrino events and is relevant only for the sufficiently small data event statistics of  $\text{RoI}_{\text{CNO}}$ , while it is negligible in  $\text{RoI}_{\text{gvc}}$ .

The value of the fit response bias in  $\text{RoI}_{\text{CNO}}$  is estimated using the Bayesian posterior distribution of  $N_\nu$  [27], which is produced through a toy-MC rejection sampling, described in summary below. The prior distribution for the number of neutrino events is chosen to be uniform between zero and the number of selected data events (2990 for Phase-I and 5974 for Phase-II + III), the prior distribution of  $\Delta r_{\text{dir}}$  is also uniform, and the prior distribution of  $g_{\text{vch}}$  is given by the measurement at the  ${}^7\text{Be}-\nu$  edge  $\text{RoI}_{\text{gvc}}$  ( $P(g_{\text{vch}}) \propto \exp(-\frac{1}{2}\Delta\chi^2(g_{\text{vch}}))$ ). The pseudodata inputs ( $N_\nu^{\text{sim}}$ ,  $g_{\text{vch}}^{\text{sim}}$ ,  $\Delta r_{\text{dir}}^{\text{sim}}$ ) are sampled from the MC signal and background  $\cos \alpha$  distributions following these model parameter prior distributions. The analysis is then performed in the same way as for the real data and results in best fit values of the pseudodata ( $N_\nu^{\text{fit}}$ ,  $g_{\text{vch}}^{\text{fit}}$ ,  $\Delta r_{\text{dir}}^{\text{fit}}$ ). The real data result now defines a multivariate Gaussian distribution  $P_{\text{accept}}(N_\nu, g_{\text{vch}}, \Delta r_{\text{dir}})$  with a mean value given by its best fit values and with a standard deviation given by the systematic uncertainty of the PMT time corrections. The sampled true values of the triplet ( $N_\nu^{\text{sim}}$ ,  $g_{\text{vch}}^{\text{sim}}$ ,  $\Delta r_{\text{dir}}^{\text{sim}}$ ) are then saved only with a probability of  $P_{\text{accept}}(N_\nu^{\text{fit}}, g_{\text{vch}}^{\text{fit}}, \Delta r_{\text{dir}}^{\text{fit}})$ , given by the best fit result of the pseudodata; otherwise, they are rejected. The resulting distributions of the true values for ( $N_\nu$ ,  $g_{\text{vch}}$ ,  $\Delta r_{\text{dir}}$ ) then correspond to their Bayesian posterior distributions. The rejection sampling of the posterior distribution corresponds to an unfolding of the fit response bias, which therefore does not represent a systematic error.

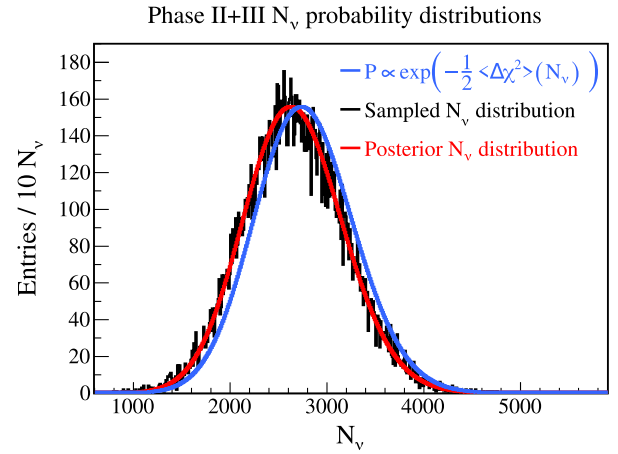


FIG. 7. Correction of the fit response bias for Phase II + III in the  $\text{RoI}_{\text{CNO}}$ . The data fit result, i.e., the likelihood  $P(\nu)$  given by the  $\Delta\chi^2$  profile of Eq. (5) and averaged over 1000 fits with different PMT time offsets, is shown in blue. The posterior distribution of 20 k pseudodata analyses, selected through rejection sampling, is shown in black. The red line corresponds to the posterior distribution that includes only the systematics from the PMT time alignment correction.

The fit response bias is illustrated in Fig. 7 for Phase II + III. The likelihood distribution  $P(N_\nu) \propto \exp(-\frac{1}{2}\Delta\chi^2(N_\nu))$ , given by the  $\chi^2$  fit of data with Eq. (5) and averaged over the 1000 fits with different PMT time offsets, is shown in blue. The black distribution is given by the simulation of 20 k pseudodata analyses, selected through the rejection sampling MC described above. The red distribution is produced by shifting  $P(N_\nu)$  by a value of  $\Delta N_\nu = -109 \pm 4$ , and this distribution is well in agreement with the black rejection sampled distribution. It is therefore used as the posterior distribution of the CID analyses. We note that for the Phase-I, the situation is similar, and the shift is found to be  $-50 \pm 4$  events.

*Inclusion of systematics.* The final result of the CID analysis for the number of solar neutrinos is given by the Bayesian posterior distribution of  $N_\nu$ , marginalized over the nuisance parameters and convoluted with the systematic uncertainties. The relevant systematic uncertainties are shown in Table II and assumed to be normally distributed.

The posterior distributions  $P(N_\nu)$  in Phase-I and Phase-II + III, including these systematics are shown in Fig. 8. The resulting number of solar neutrinos detected in the  $\text{RoI}_{\text{CNO}}$  is  $N_\nu = 643_{-224}^{+235}(\text{stat})_{-30}^{+37}(\text{sys})$  for Phase-I and  $N_\nu = 2719_{-494}^{+518}(\text{stat})_{-83}^{+85}(\text{sys})$  for Phase-II + III, including all systematics and correcting for the fit response bias. The quoted uncertainties are calculated from the posterior distributions using an 68% equal-tailed credible interval (CI). The one-sided zero neutrino hypothesis can be excluded

TABLE II. Systematic uncertainties on the number of solar neutrino events  $N_\nu$  in  $\text{RoI}_{\text{CNO}}$ , relative to the best fit value. The uncertainty from  $pep + {}^8\text{B}$ - $\nu$  constraint is relevant only for  $N_{\text{CNO}}$ . The last two rows are relevant only for the CNO- $\nu$  rate ( $R_{\text{CNO}}$ ) calculation.

Source of uncertainty	Phase-I (%)	Phase-II + III (%)
For $N_\nu$		
PMT selection	1.3	0.6
PMT time corrections	4.2	2.4
Low number of signal events	2.2	...
CNO- $\nu$ vs $pep$ - $\nu$ MC	2.2	2.0
For $N_{\text{CNO}}$		
$pep + {}^8\text{B}$ - $\nu$ constraint	4.6	1.8
For $R_{\text{CNO}}$		
Fiducial mass	$^{+0.2}_{-1.2}$	$^{+0.2}_{-1.2}$
Fraction of CNO- $\nu$ in $\text{RoI}$	1.4	1.4

with  $P(N_\nu = 0) = 2.8 \times 10^{-5}$  ( $\sim 4.2\sigma$ ) for Phase-I and  $P(N_\nu = 0) = 6.4 \times 10^{-11}$  ( $\sim 6.5\sigma$ ) for Phase-II + III.

*CID results on CNO.* The interpretation of the CID results requires the correct treatment of the physical boundaries of the analysis, i.e.,  $0 \leq N_\nu \leq 2990$  (5974) for Phase-I (Phase-II + III), respectively. This is done in a Bayesian interpretation, based on the posterior distribution  $P(N_\nu)$  shown in Fig. 8.

Next, the distribution of the number of CNO- $\nu$  events is estimated by constraining the expected number of  $pep$  and  ${}^8\text{B}$  neutrino events ( $N_{pep+{}^8\text{B}}$ ) where the constraint on the number of  $pep$  neutrinos uses the SSM

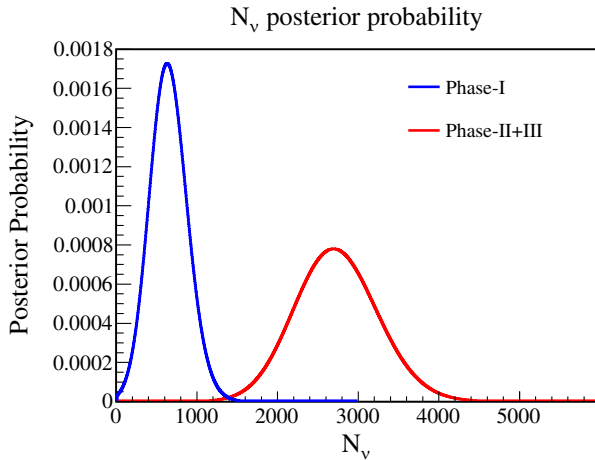


FIG. 8. The CID measured posterior probability distributions for the number of solar neutrinos  $N_\nu$  in the  $\text{RoI}_{\text{CNO}}$  for Phase-I (blue) and Phase-II + III (red). All systematic effects are included.

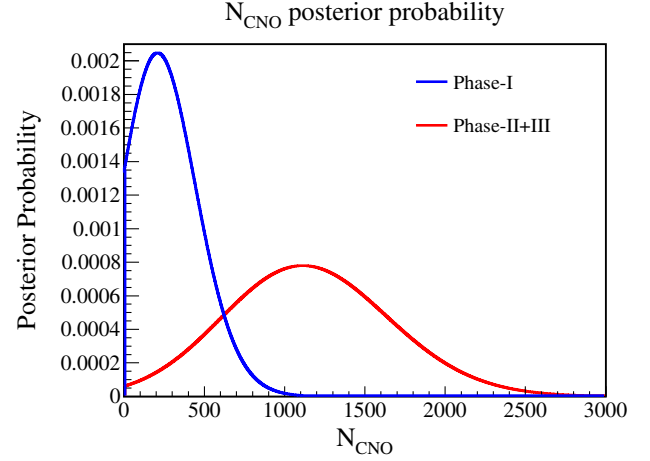


FIG. 9. The CID measured posterior probability for the number of CNO- $\nu$  events after constraining  $pep$  and  ${}^8\text{B}$  neutrinos for Phase-I (blue) and Phase-II + III (red). All systematic effects are included.

predictions [2], and  ${}^8\text{B}$  is constrained using the high precision flux measurement of Super-Kamiokande [6] including model uncertainties, the difference between HZ-SSM and LZ-SSM predictions, as well as the Borexino FV and energy systematic uncertainties from Table II. This is done through the convolution of the  $N_\nu$  posterior distributions from Fig. 8 with the predicted  $P(N_{pep+{}^8\text{B}})$  probability distribution:  $P(N_{\text{CNO}}) = P(N_\nu) * P(-N_{pep+{}^8\text{B}})$ . The resulting  $P(N_{\text{CNO}})$  posterior distributions are shown in Fig. 9. The CID measurement for the number of CNO- $\nu$  events is then  $N_{\text{CNO}} = 270^{+218}_{-169}(\text{stat})^{+33}_{-25}(\text{sys})$  for Phase-I and  $N_{\text{CNO}} = 1146^{+518}_{-486}(\text{stat})^{+92}_{-89}(\text{sys})$  for Phase-II + III, where the uncertainty corresponds to the equal-tail 68% CI within the physical boundaries, including all systematics.

It has been observed that Phase-I and Phase-II + III do not show prohibitively different behavior for the full CID analysis chain, and the MC model is well able to reproduce the data  $\cos \alpha$  histograms for both phase selections and for each selected energy region. It is then reasonable to combine the conditionally independent results of Phase-I and Phase-II + III, through the convolution of both posterior distributions  $P(N_{\text{CNO}})^{\text{I+II+III}} = P(N_{\text{CNO}})^{\text{I}} * P(N_{\text{CNO}})^{\text{II+III}}$ . The probability that exactly zero CNO- $\nu$  events contribute to the measured data CID  $\cos \alpha$  distribution is  $P(N_{\text{CNO}} = 0) = 1.35 \times 10^{-3}$  for Phase-I,  $P(N_{\text{CNO}} = 0) = 5.87 \times 10^{-5}$  for Phase-II + III, and  $P(N_{\text{CNO}} = 0) = 7.93 \times 10^{-8}$  for the combined result. This corresponds to a one-sided exclusion of the zero-CNO hypothesis at about  $5.3\sigma$  credible interval for the combination of Phase-I and Phase-II + III.

The CNO- $\nu$  rate probability density function is calculated from the measured posterior distribution of CNO- $\nu$  events, using the exposure of the respective phases.

TABLE III. CID CNO- $\nu$  results with systematic uncertainties.

CID results	$P(N_{\text{CNO}} = 0)$	$R_{\text{CNO}} \left[ \frac{\text{cpd}}{100 \text{ tonnes}} \right]$
Phase-I	$1.35 \times 10^{-3}$	$6.4^{+5.2}_{-4.1}$
Phase-II + III	$5.87 \times 10^{-5}$	$7.3^{+3.4}_{-3.2}$
Combined	$7.93 \times 10^{-8}$	$7.2^{+2.8}_{-2.7}$

The effective exposure is given by the product of the fiducial mass, the detector live time, the TFC-exposure, the trigger efficiency, and the fraction of CNO- $\nu$  events within the selected energy region. The final CID result for the CNO- $\nu$  rate, using the full dataset of Phase-I + Phase-II + III, is  $R_{\text{CNO}}^{\text{CID}} = 7.2 \pm 2.5(\text{stat}) \pm 0.4(\text{sys})^{+1.1}_{-0.8}(\text{nuisance})$  cpd/100 tonnes =  $7.2^{+2.8}_{-2.7}$  cpd/100 tonnes. The quoted uncertainties now also show the systematic uncertainties from Table II separately from the influence of the nuisance parameters  $g_{\nu\text{ch}}$  and  $\Delta r_{\text{dir}}$ . The quoted statistical uncertainty corresponds to a hypothetical, perfect calibration of these CID nuisance parameters. The results are summarized in Table III.

These CID results are well in agreement with the HZ-SSM prediction of  $(4.92 \pm 0.78)$  cpd/100 tonnes ( $0.6\sigma$ ), while the LZ-SSM prediction  $(3.52 \pm 0.52)$  cpd/100 tonnes ( $1.1\sigma$ ) is 1.7 times less likely to be true, given the results of the Borexino CID analysis. The corresponding CNO- $\nu$  rate posterior distribution is shown in Fig. 10.

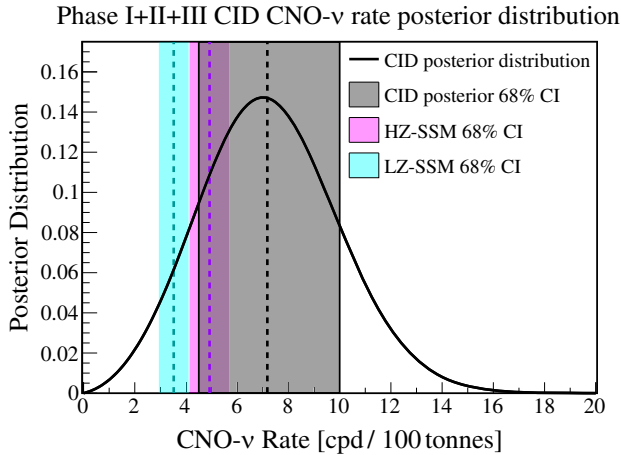


FIG. 10. The combined CID Phase-I + Phase-II + III CNO- $\nu$  rate posterior distribution is shown in red. The blue, violet, and gray bands show the 68% CI, for the low metallicity SSM B16-AGSS09met [ $(3.52 \pm 0.52)$  cpd/100 tonnes], the high metallicity SSM B16-GS98 [ $(4.92 \pm 0.78)$  cpd/100 tonnes] predictions [2,31], and the combined CID result, respectively. All systematic effects are included.

#### IV. COMBINED CID AND MULTIVARIATE ANALYSIS

In this section, we combine the CID analysis with the standard multivariate fit of Phase-III to improve the result on CNO neutrinos. This is done by including the posterior distributions of solar neutrinos from the CID analysis, shown in Fig. 8, in the multivariate analysis likelihood. The multivariate minimization included the CID neutrino posterior distributions as external likelihood terms after statistical subtraction of the subdominant  $^8\text{B}$  neutrinos and the conversion to neutrino interaction rate. Following this procedure, two multiplicative pull terms constraining the number of CNO and  $pep$  neutrino events are used: The first one is related to the Phase-I ( $\mathcal{L}_{\text{CID}}^{\text{P-I}}$ ), while the second one refers to Phase-II + III datasets ( $\mathcal{L}_{\text{CID}}^{\text{P-II+III}}$ ).

The overall combined likelihood used for this analysis becomes

$$\mathcal{L}_{\text{MV+CID}} = \mathcal{L}_{\text{MV}} \cdot \mathcal{L}_{\text{pep}} \cdot \mathcal{L}_{^{210}\text{Bi}} \cdot \mathcal{L}_{\text{CID}}^{\text{P-I}} \cdot \mathcal{L}_{\text{CID}}^{\text{P-II+III}}, \quad (7)$$

where the first three terms correspond to an improved version of the standard multivariate analysis described in [19]. This approach couples the one-dimensional Poisson likelihood for the TFC-Tagged dataset with a two-dimensional one (energy and radius) for the TFC-subtracted to enhance the separation between signal and backgrounds. We have improved the binning optimization and used an updated version of Monte Carlo.

The  $pep$  neutrinos interaction rate is constrained with 1.4% precision to the  $2.74 \pm 0.04$  cpd/100 tonnes value, by combining the standard solar model predictions [2], the most current flavor oscillation parameters set [28], and the solar neutrino data [29,30]. This constraint is applied with the Gaussian pull term  $\mathcal{L}_{\text{pep}}$ . An upper limit on the  $^{210}\text{Bi}$  rate of  $(10.8 \pm 1.0)$  cpd/100 tonnes is applied with the half Gaussian term  $\mathcal{L}_{^{210}\text{Bi}}$ . This upper limit is obtained from the rate of the  $^{210}\text{Bi}$  daughter  $^{210}\text{Po}$  (see [4,19] for more details).

##### A. Results

As in [19], the energy RoI for the multivariate analysis is  $0.32 \text{ MeV} < T_e < 2.64 \text{ MeV}$  for electron recoil kinetic energy. The reconstructed energy spectrum scale is quantified in the  $N_h$  estimator, representing total number of detected hits for a given event (see Sec. II). The dataset is the same one analyzed in [19], in which the exposure amounts to  $1431.6 \text{ days} \times 71.3 \text{ tonnes}$ .

Along with CNO solar neutrinos, the free parameters of the fit are divided into three categories: internal ( $^{85}\text{Kr}$  and  $^{210}\text{Po}$ ) and external ( $^{208}\text{Tl}$ ,  $^{214}\text{Bi}$ , and  $^{40}\text{K}$ ) backgrounds, cosmogenic backgrounds ( $^{14}\text{C}$ ,  $^6\text{He}$ , and  $^{10}\text{C}$ ), and solar neutrinos ( $^7\text{Be}$ ). Since  $^8\text{B}$  solar neutrinos exhibit a flat and marginal contribution, the corresponding interaction rate is fixed at high-metallicity expectations from the solar standard model. As discussed in Eq. (7), the interaction rates of  $pep$

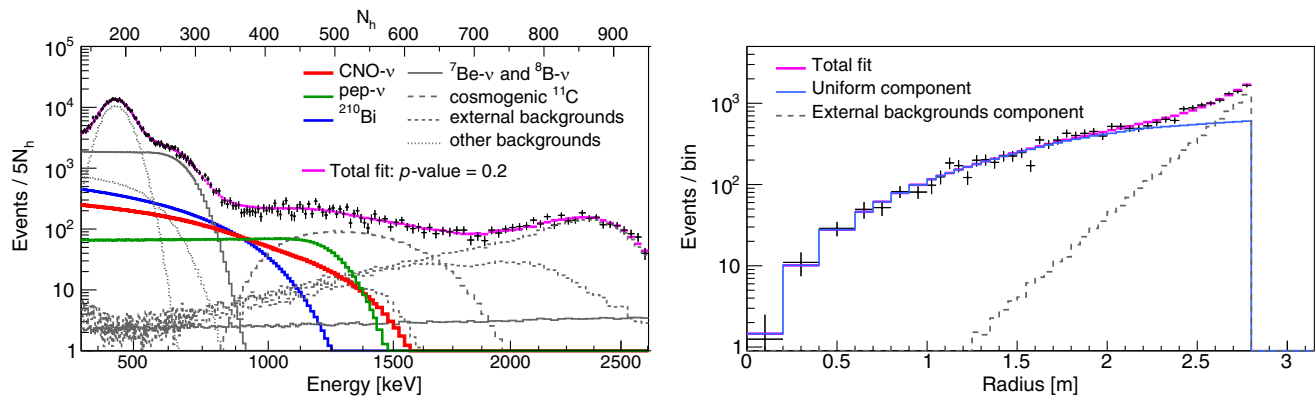


FIG. 11. Multivariate fit results for the TFC-subtracted dataset, projected over the energy (top panel) and the radius (bottom panel) dimensions. For both projections, the sum of the individual components from the fit (magenta) is superimposed on the data (gray points). CNO neutrinos,  $^{210}\text{Bi}$ , and  $pep$  neutrinos contributions are displayed in solid red, dashed blue, and dotted green lines, respectively, while the other spectral components ( $^7\text{Be}$  and  $^8\text{B}$  neutrinos, other backgrounds) are shown in gray. The analysis has been performed using  $N_h$  as energy estimator, and the conversion to keV energy scale was performed only for the plotting purposes. The radial fit components, which are the uniform and the external backgrounds contributions, are shown in solid blue and dashed gray lines, respectively.

neutrinos and  $^{210}\text{Bi}$  background are constrained with likelihood pull terms, and CID results reported in Sec. III E are accounted for as additional external constraints. The result of the fit for the energy and radial projections is shown in Fig. 11.

The multivariate fit returns an interaction rate of CNO neutrinos of  $6.7_{-0.7}^{+1.2}$  cpd/100 tonnes (statistical error only). The agreement between the model and data is quantified with a  $p$  value of 0.2.

To account for sources of systematic uncertainty, the same Monte Carlo method described in [4,19] has been adopted. In a nutshell, hundred thousand Monte Carlo pseudoexperiments were generated, including relevant effects able to introduce a systematic error, such as the energy response nonlinearity and nonuniformity, the time variation of the scintillator light yield, and the different theoretical models for the  $^{210}\text{Bi}$  spectral shape. The analysis is performed on these pseudodatasets assuming the standard response to study how this impacts the final result on CNO, yielding a total systematic uncertainty of  $^{+0.31}_{-0.24}$  cpd/100 tonnes. Other sources of systematic error are included in the estimation of the upper limit on  $^{210}\text{Bi}$  contamination, as discussed more in detail in [4,19].

The negative log-likelihood profile as a function of the CNO rate is reported in Fig. 12. The solid and dashed black lines show the results with and without systematic uncertainty, respectively. The result without CID constraint reported in [19] is included (gray dash-dotted line), for comparison. The improvement is clear especially for the upper value of the CNO rate. The CNO interaction rate is extracted from the 68% quantile of the likelihood profile convoluted with the resulting systematic uncertainty, as  $R^{\text{MV}+\text{CID}}(\text{CNO}) = 6.7_{-0.8}^{+1.2}$  cpd/100 tonnes. The significance to the non-CNO hypothesis reaches about  $8\sigma$

CL, while the resulting CNO flux at Earth is  $\Phi(\text{CNO}) = 6.7_{-0.8}^{+1.2} \times 10^8 \text{ cm}^{-2} \text{ s}^{-1}$ . Following the same procedure used in [19], we use this result together with the  $^8\text{B}$  flux obtained from the global analysis of all solar data to determine the abundance of C + N with respect to H in the Sun with an improved precision, for which we find  $N_{\text{CN}} = 5.81_{-0.94}^{+1.22} \times 10^{-4}$ . This error includes both the statistical uncertainty due to the CNO measurement and the systematic errors due to the additional contribution

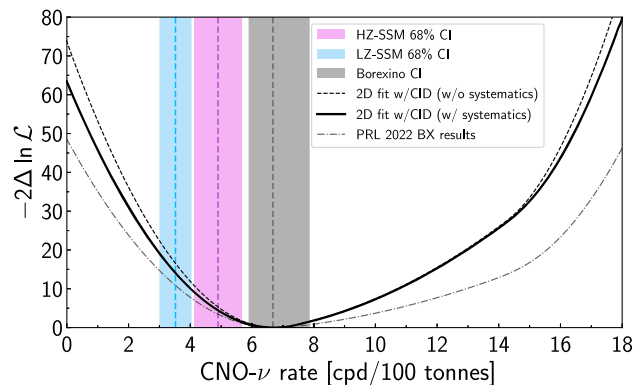


FIG. 12. CNO- $\nu$  rate negative log-likelihood ( $-2\Delta \ln \mathcal{L}$ ) profile obtained from the two-dimensional multivariate spectral fit combined with the CID analysis constraint, with and without folding in the systematic uncertainties (black dashed and solid lines, respectively). The gray dash-dotted line shows the same profile obtained in the previously published analysis without CID constraint [19]. The blue, violet, and gray vertical bands show 68% confidence intervals (CI) for the low-metallicity SSM B16-AGSS09met ( $3.52 \pm 0.52$  cpd/100 tonnes) and the high-metallicity SSM B16-GS98 ( $4.92 \pm 0.78$  cpd/100 tonnes) predictions [2,31], and the new Borexino result including systematic uncertainty, respectively.

of the SSM inputs, to the  $^8\text{B}$  flux measurement, and to the  $^{13}\text{N}/^{15}\text{O}$  fluxes ratio. Similar to what was inferred from our previous publication, this result is in agreement with the high metallicity measurements [14,15] and features a  $2\sigma$  tension with low metallicity ones [16–18]. Similarly, if we combine the new CNO result with the other Borexino results on  $^7\text{Be}$  and  $^8\text{B}$  in a frequentist hypothesis test based on a likelihood ratio test statistics, we find that, assuming the HZ-SSM to be true, our data disfavors LZ-SSM at  $3.2\sigma$  level.

## V. CONCLUSIONS

In this work, we have presented the results on CNO solar neutrinos obtained using the CID technique.

We have shown that the CID technique can be used to extract the CNO signal without any *a priori* assumptions on the backgrounds, in particular, that of  $^{210}\text{Bi}$ . The Phase-I (May 2007 to May 2010, 740.7 days) and Phase-II + III (December 2011 to October 2021, 2888.0 days) datasets have been analyzed independently to investigate possible variations of the detector response over time. By adopting the Bayesian statistics, we have combined the conditionally independent results of Phase-I and Phase-II + III: The resulting CNO rate obtained with CID only is  $7.2^{+2.8}_{-2.7}$  cpd/100 tonnes. The non-CNO hypothesis including the *pep* constraint only is rejected at  $5.3\sigma$  level. This result, albeit less precise than the one published by Borexino using the standard multivariate analysis, is the first obtained without the application of a  $^{210}\text{Bi}$  constraint.

We have also obtained an improved CNO solar neutrino result by combining the standard multivariate analysis with the CID technique. The CID technique helps in separating the solar signal from nonsolar backgrounds, improving the significance and precision of the CNO measurement with respect to the result previously published by Borexino.

The resulting CNO interaction rate is  $6.7^{+1.2}_{-0.8}$  cpd/100tonnes and the significance against the absence of a CNO signal, considered as the null hypothesis, is about  $8\sigma$ . The C + N abundance with respect to H is calculated from this result following the procedure adopted in [19] and is found to be  $N_{\text{CN}} = 5.81^{+1.22}_{-0.94} \times 10^{-4}$ , compatible with the SSM-HZ metallicity measurements.

In conclusion, we have shown that the directional information of the Cherenkov radiation can be effectively combined with the spectral information coming from scintillation for solar neutrino studies. This combined detection approach provides a measurement that is more powerful than the individual methods on their own. The sensitivity of the CID method could be significantly improved in future liquid scintillator-based detectors by optimizing the Cherenkov-to-scintillation ratio and by performing dedicated calibrations campaigns.

## ACKNOWLEDGMENTS

We acknowledge the generous hospitality and support of the Laboratori Nazionali del Gran Sasso (Italy). The Borexino program is made possible by funding from Istituto Nazionale di Fisica Nucleare (INFN) (Italy), National Science Foundation (NSF) (USA), Deutsche Forschungsgemeinschaft (DFG, Project ID 39083149), and recruitment initiative of Helmholtz-Gemeinschaft (HGF) (Germany), Russian Foundation for Basic Research (RFBR) (Grant No. 19-02-00097A), Russian Science Foundation (RSF) (Grant No. 21-12-00063) and Ministry of Science and Higher Education of the Russian Federation (Project FSWU-2023-0073) (Russia), and Narodowe Centrum Nauki (NCN) (Grant No. UMO 2017/26/M/ST2/00915) (Poland). We gratefully acknowledge the computing services of Bologna INFN-CNAF data centre and U-Lite Computing Center and Network Service at LNGS (Italy).

- 
- [1] J. N. Bahcall, *Neutrino Astrophysics* (Cambridge University Press, Cambridge, England, 1989).
  - [2] N. Vinyoles, A. M. Serenelli, F. L. Villante, S. Basu, J. Bergström, M. C. Gonzalez-Garcia, M. Maltoni, C. Peña-Garay, and N. Song, *Astrophys. J.* **835**, 202 (2017).
  - [3] M. Salaris and S. Cassisi, *Evolution of Stars and Stellar Populations* (John Wiley & Sons, Ltd, New York, 2005).
  - [4] Borexino Collaboration, *Nature (London)* **587**, 577 (2020).
  - [5] Borexino Collaboration, *Nature (London)* **562**, 505 (2018).
  - [6] K. Abe *et al.* (Super-Kamiokande Collaboration), *Phys. Rev. D* **94**, 052010 (2016).
  - [7] M. Anderson *et al.* (SNO+ Collaboration), *Phys. Rev. D* **99**, 012012 (2019).
  - [8] B. T. Cleveland, T. Daily, R. Davis, Jr., J. R. Distel, K. Lande, C. K. Lee, P. S. Wildenhain, and J. Ullman (Homestake Collaboration), *Astrophys. J.* **496**, 505 (1998).
  - [9] J. N. Abdurashitov *et al.* (SAGE Collaboration), *Phys. Rev. C* **80**, 015807 (2009).
  - [10] F. Kaether, W. Hampel, G. Heusser, J. Kiko, and T. Kirsten, *Phys. Lett. B* **685**, 47 (2010).
  - [11] T. Araki *et al.* (KamLAND Collaboration), *Phys. Rev. Lett.* **94**, 081801 (2005).
  - [12] Q. R. Ahmad *et al.* (SNO Collaboration), *Phys. Rev. Lett.* **89**, 011301 (2002).
  - [13] G. Bellini *et al.* (Borexino Collaboration), *Phys. Rev. Lett.* **107**, 141302 (2011).

- [14] N. Grevesse and A. Sauval, *Space Sci. Rev.* **85**, 161 (1998).
- [15] E. Magg *et al.*, *Astron. Astrophys.* **661**, A140 (2022).
- [16] E. Caffau, H.-G. Ludwig, M. Steffen, B. Freytag, and P. Bonifacio, *Sol. Phys.* **268**, 255 (2010).
- [17] M. Asplund, N. Grevesse, A. J. Sauval, and P. Scott, *Annu. Rev. Astron. Astrophys.* **47**, 481 (2009).
- [18] M. Asplund, A. M. Amarsi, and N. Grevesse, *Astron. Astrophys.* **653**, A141 (2021).
- [19] S. Appel *et al.* (Borexino Collaboration), *Phys. Rev. Lett.* **129**, 252701 (2022).
- [20] M. Agostini *et al.* (Borexino Collaboration), *Phys. Rev. D* **105**, 052002 (2022).
- [21] M. Agostini *et al.* (Borexino Collaboration), *Phys. Rev. Lett.* **128**, 091803 (2022).
- [22] G. Alimonti *et al.* (Borexino Collaboration), *Nucl. Instrum. Methods Phys. Res., Sect. A* **600**, 568 (2009).
- [23] G. Bellini *et al.* (Borexino Collaboration), *Phys. Rev. D* **89**, 112007 (2014).
- [24] M. Agostini *et al.* (Borexino Collaboration), *Astropart. Phys.* **97**, 136 (2018).
- [25] H. Back *et al.* (Borexino Collaboration), *J. Instrum.* **7**, P10018 (2012).
- [26] K. Abe *et al.* (Super-Kamiokande Collaboration), *Phys. Rev. D* **94**, 052010 (2016).
- [27] G. D'Agostini, *Rep. Prog. Phys.* **66**, 1383 (2003).
- [28] F. Capozzi, E. Di Valentino, E. Lisi, A. Marrone, A. Melchiorri, and A. Palazzo, *Phys. Rev. D* **104**, 083031 (2021).
- [29] D. Vescovi, C. Mascaretti, F. Vissani, L. Piersanti, and O. Straniero, *J. Phys. G* **48**, 015201 (2020).
- [30] J. Bergstrom, M. C. Gonzalez-Garcia, M. Maltoni, C. Pena-Garay, A. M. Serenelli, and N. Song, *J. High Energy Phys.* **03** (2016) 132.
- [31] M. Agostini *et al.* (Borexino Collaboration), *Eur. Phys. J. C* **80**, 1091 (2020).